JOURNAL OF AIRCRAFT
Vol. 46, No. 1, January–February 2009

Strain-Energy Release Rate Analysis of Adhesive-Bonded Composite Joints with Prescribed Interlaminar Crack

Alireza Chadegani* and Chihdar Yang†
Wichita State University, Wichita, Kansas 67260-0044
and
Eugene Dan-Jumbo‡
Northrop Grumman Corporation, San Diego, California 92150

DOI: 10.2514/1.37513

Composite materials together with adhesive bonding have been increasingly used in the aviation industry. Delamination is among the critical failure modes in fiber-reinforced laminated composite structures. This paper presents an analytical approach by taking into account the first-ply failure in adhesive-bonded composite joints subjected to axial tension. The American Society for Testing and Materials (ASTM) D3165 standard test specimen geometry is followed for model development derivations. The field equations, in terms of displacements within the joint, are formulated by using the first-order, shear-deformable, laminated plate theory together with kinematics relations and force equilibrium conditions. The stress distributions for the adherends and adhesive are determined after the appropriate boundary and loading conditions are applied and the equations for the field displacements are solved. The equivalent forces at the tip of the prescribed interlaminar crack are obtained based on interlaminar stress distributions. The strain-energy release rate of the crack is then determined by using the virtual crack closure technique. The system of second-order differential field equations is solved to provide the adherend and adhesive stresses using the symbolic computation tool, Maple 9.52. Finite element analyses using the *J* integral as well as the virtual crack closure technique are performed to verify the developed analytical model. Finite element analyses are conducted using the commercial finite element analysis software ABAQUS 6.5-1. Results are determined using the analytical method correlated properly with the results from the finite element analyses.

Nomenclature

$A_{11}, A_{11}^U, A_{11}^L$	=	in-plane modulus per unit width, kN/m
$A_{55}, A_{55}^U, A_{55}^L$	=	transverse modulus per unit width, kN/m
a	=	prescribed crack length, m
$B_{11}, B_{11}^U, B_{11}^L$	=	coupling modulus per unit width, kN
b	=	virtual crack extension length, m
$D_{11}, D_{11}^U, D_{11}^L$	=	flexural modulus per unit width, kN · m
E_a	=	adhesive Young's modulus, kPa
G_a	=	adhesive shear modulus, kPa
G_I	=	mode I strain-energy release rate, N/m
G_{II}	=	mode II strain-energy release rate, N/m
G_T	=	total strain-energy release rate, N/m
G_{xz}	=	adherend x–z plane shear modulus, kPa
h_2	=	adherend ply thickness, m
h^U, h^L, h	=	adherend thickness, m
J	=	J-integral value, N/m
k_s, k_s^U, k_s^L	=	shear correction factor
l_n	=	notch length of ASTM D3165 specimen, m
l_o	=	overlap length before crack is initiated
M_y, M_y^U, M_y^L	=	bending moment per unit width, kN
N_x, N_x^U, N_x^L	=	normal stress resultants per unit width, kN/m
P	=	applied tensile force per unit width, N/m
Q_z, Q_z^U, Q_z^L	=	transverse shear stress resultant per unit width, kN/m
q_a	=	adhesive peel stress, kPa
q_i	=	interlaminar peel stress, kPa
u^U, u^L	=	x-directional displacement, m
u^o, u^{oU}, u^{oL}	=	midplane x-directional displacement, m
υ_a	=	adhesive Poisson's ratio
w, w^U, w^L	=	z-directional displacement, m
$\varepsilon_x, \varepsilon_z, \gamma_{xz}$	=	adhesive strains
η	=	adhesive thickness, m
σ_x	=	adhesive normal stress, kPa
τ_a	=	adhesive shear stress, kPa
τ_i	=	interlaminar shear stress, kPa
ψ, ψ^U, ψ^L	=	bending slope, rad

I. Introduction

ADVANCED composite materials and adhesive-bonding technology have been widely applied in aerospace/aircraft structures because of their high strength-to-weight ratio and excellent resistance to corrosion. In many applications, bolted joints have been replaced by adhesive-bonded joints because of the weight penalty and corrosion problems associated with bolted joints. One of the major issues in applications of adhesive-bonded composite joints is the prediction of damage and failure mechanisms. A complete investigation of the failure modes leads to an efficient and durable joint design.

Delamination always refers to interlaminar failure, which initiates by a crack in the matrix and may lead to fiber separation. Therefore, a matrix crack occurs within laminates where the fibers are parallel to the load direction. Based on the direction of crack propagation, edge or local delaminations have been categorized. Edge delamination occurs at the load-free edges of the laminate, whereas local delamination initiates from a transverse matrix crack. It has been observed in simple tension tests of a uniform rectangular cross-section specimen that delaminations start along the load-free edges and propagate normal to the load direction [1]. Many research articles have been devoted to the study of matrix cracking in

Presented at the 49th AIAA/ASME/ASCE/AHS/ASC Structures, Structural Dynamics, and Materials Conference, Schaumburg, Illinois, 7–10 April 2008; received 12 March 2008; revision received 23 July 2008; accepted for publication 1 September 2008.

*Graduate Research Assistant, Department of Aerospace Engineering; axchadegani@wichita.edu. Student Member AIAA.
†Associate Professor and Airbus Fellow of Aerospace Engineering Department; charles.yang@wichita.edu.
‡Senior Principal Engineer/Scientist; eugene.dan-jumbo@ngc.com.

laminated composite plates, although most have developed finite element (FE) approaches. Moreover, several researchers have studied the first-ply failure of laminated composite plates analytically, whereas first-ply failure in laminated composite-bonded joints rarely has been discussed. Accurate predictions of a first-ply failure mechanism and load are essential in understanding the failure process as well as reliability of laminated composite-bonded joints. In a composite-bonded joint, failure typically occurs in the first ply of the adherend near the stress singularity.

Delaminations near free edges, holes, ply drops, and notches have been noticed in laminated composites in service. In practical composite structures, delamination is a mixed-mode fracture process, which includes mode I or the opening mode, mode II or the shearing mode, and mode III or the tearing mode. The growth process of edge delaminations and local delamination is often modeled by a fracture-mechanics approach leading to the calculation of a strain-energy release rate (SERR), which can account for various geometries and loading conditions. In combination with an appropriate failure criterion, the SERR can be used as a means to predict the failure load of the structure. Several methods are available in the literature for calculating the SERR: finite element analysis and the complex variable stress potential approach [1]. In a research study conducted by Yang et al. [2] on adhesive-bonded joints, it was concluded that the fracture-mechanics approach would be an effective method for predicting the load-carrying capacity of bonded joints.

Earlier studies of adhesive-bonded joints can be found in extensive reviews given by Kutscha [3], Kutscha and Hofer [4], Matthews et al. [5], and Vinson [6]. Yang and Pang [7] derived an analytical model that provided the stress distributions of adhesive-bonded single-lap composite joints subjected to axial tension. Huang et al. [8] and Yang et al. [9] also derived an elastic-plastic model for adhesive-bonded single-lap composite joints. Their approaches included important capabilities such as the asymmetry of the adherend laminates and the effects due to transverse shear deformation. An existing crack is usually assumed to be in a joint when conducting a fracture analysis. In a report published in 2002, Krueger [10] described the virtual crack closure technique (VCCT), including its history, approach, and applications in conjunction with finite element analysis. Davidson et al. [11] published a series of papers that employed the classical plate theory version of the VCCT to predict the strain-energy release rate of mixed-mode delamination in composite laminates. A crack-tip force method was derived by Park and Sankar [12] to compute the strain-energy release rate in delaminated beams and plates. Kim and Kong [13] proposed a simplified method for determining the strain-energy release rate of free-edge delamination in composites using the classical laminated plated theory.

Finite element methods play a significant role in structural analysis and have been widely used to study the adhesive-bonded composite joint. Wang et al. [14] applied the VCCT to calculate the strain-energy release rate of cracked composite panels with nonlinear deformation. Wei et al. [15] presented an improved VCCT to determine the energy release rate using a three-step analysis. Yang et al. [16,17] developed finite element models using the finite element software, ABAQUS^{TM} [18] to estimate the J integral of an adhesive-bonded joint with a crack. Although finite element analysis methods are capable of solving problems with various types of materials and complicated geometrical configurations, analytical solutions offer advantageous performance and solution, especially with parametric analyses and optimization. Interlaminar fracture in composites using the sublaminate approach has been studied by Armanios and Rehfield [19–21] and Rehfield et al. [22], in spite of simplifications related to the case study.

The objective of the present paper is to describe an analytical fracture-mechanics method that can be used to determine the strain-energy release rate from first-ply failure in an adhesive-bonded single-lap composite joint. The prescribed interlaminar crack is assumed to be initiated at the corner of the notch where stress singularity exists, adjacent to the overlap region in the transverse direction, resulting from fiber breakage and matrix cracking. The crack consequently propagates into the interface of the first ply of the adherend and delaminates fibers from the parent adherend.

Linear-elastic material properties as well as small displacements are assumed for both the adhesive and adherends to make the analytical approach feasible. In the following sections, step-by-step approaches and formulation development using laminated anisotropic plate theory for the adherend and interlaminar stress distributions are discussed. The American Society for Testing and Materials (ASTM) D3165 [23] specimen geometry is used in the model derivations. The analytical solutions are determined using the symbolic computation tool Maple 9.52 [24]. Results from the analytical model are verified by finite element analysis using ABAQUS 6.5-1 [18].

II. Model Development

Details of the analytical method for determining the strain-energy release rate of adhesive-bonded single-lap composite joints with a prescribed interlaminar crack are based on the laminated plate theory version of Irwin's virtual crack method [10]. The SERR is derived in terms of the forces and moment at the crack tip: N_C, Q_C, and M_C. These forces and moment at the crack tip are determined from the linear-elastic shear and peel stress distributions at the first-ply adherend interface within the overlap area. Therefore, a description of the stress state in the pre- and postpropagation specimen geometry is required before an estimate of the strain-energy release rate can be obtained. A summary of the methodology used to derive the equations for determining the required stress and displacement fields in an adhesive-bonded joint is presented in this section.

An adhesive-bonded single-lap joint with the standard geometry of an ASTM D3165 specimen and an applied tensile load P per unit width is shown in Fig. 1. Here, the joint is divided into six regions for convenience in the model development, where regions 1, 4, and 6 consist of two adherends and a thin-adhesive layer, regions 2 and 5 represent two notches, and region 3 is also assumed to be due to first-ply failure of the laminate in the overlap area and its corresponding geometry discontinuity. Region 4 is the bonded-joint overlap area where the applied mechanical loads are transferred from one adherend to the other and is also the area on which joint strength is typically based.

The step-by-step solution procedure can be summarized as follows:

1) Divide the model into adherend portions according to the ASTM D3165 specimen geometry and derive the kinematics relations for each adherend portion.

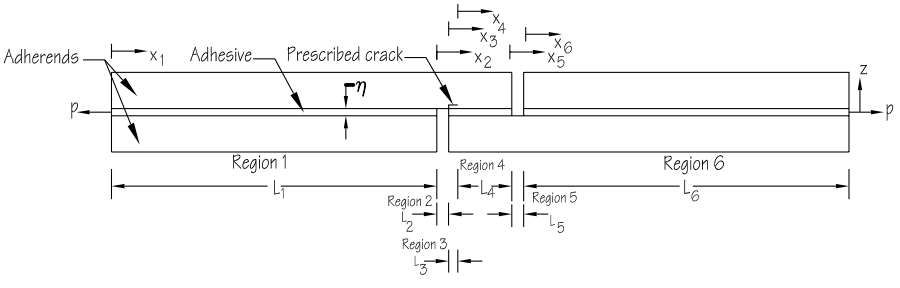

Fig. 1 ASTM D3165 specimen geometry.

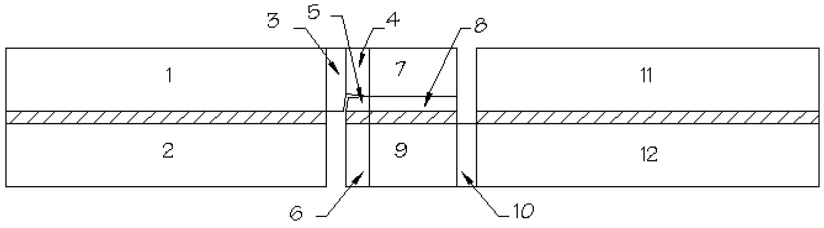

Fig. 2 Discretized model with 12 adherend portions.

2) Write force and moment equilibriums for each adherend portion with respect to sign convention.

3) Derive equations for the adhesive and interlaminar stresses using the kinematics of adherends.

4) Specify boundary conditions according to the loading status and displacement constraints.

5) Find the equivalent crack-tip forces and moment and propagate the crack to find displacement distributions.

6) Apply the VCCT formulation to calculate the SERR.

A. Adherend Formulation

The specimen is discretized into 12 adherend portions from left to right, as shown in Fig. 2. The general formulas for the adherend portions are the same for all adherend portions, except for adherend portions 5 and 8. The displacement fields of the adherend are described by the laminated anisotropic plate theory.

1. Adherend Portions 1–4, 6, 7, and 9–12

Based on the first-order laminated plate theory, the displacement fields for the adherend portions 1–4, 6, 7, and 9–12 can be written as

$$u = u^o(x) + z\psi(x) \tag{1}$$

$$w = w(x) \tag{2}$$

where the superscript o represents the midplane displacement, z is measured from the midplane of each adherend portion, and ψ is the corresponding bending slope. Considering the given displacement functions and the strain-displacement relations yields the normal strain ε_x and shear strain γ_{xy} for each adherend portion as

$$\varepsilon_x = \frac{\mathrm{d}u}{\mathrm{d}x} = \frac{\mathrm{d}u^o(x)}{\mathrm{d}x} + z\frac{\mathrm{d}\psi(x)}{\mathrm{d}x} \tag{3}$$

$$\gamma_{xy} = \frac{\mathrm{d}w}{\mathrm{d}x} + \frac{\mathrm{d}u}{\mathrm{d}z} = \frac{\mathrm{d}w(x)}{\mathrm{d}x} + \psi(x) \tag{4}$$

Therefore, based on the classical laminate theory, the relationships among stress resultants, strain, and bending slope can be formulated. Furthermore, using the extensional stiffness $[A]$, the coupling stiffness $[B]$, and the bending stiffness $[D]$ for orthotropic laminates, the normal stress resultant N_x, bending moment for unit width M_y, and transverse shear stress resultant Q_z can be obtained as

$$N_x = A_{11}\frac{\mathrm{d}u^o(x)}{\mathrm{d}x} + B_{11}\frac{\mathrm{d}\psi(x)}{\mathrm{d}x} \tag{5}$$

$$M_y = B_{11}\frac{\mathrm{d}u^o(x)}{\mathrm{d}x} + D_{11}\frac{\mathrm{d}\psi(x)}{\mathrm{d}x} \tag{6}$$

$$Q_z = k_s A_{55}\left[\psi(x) + \frac{\mathrm{d}w(x)}{\mathrm{d}x}\right] \tag{7}$$

where k_s is the shear correction factor, and A_{ij}, B_{ij}, and D_{ij} terms are taken from the common extensional, bending, and extensional-bending coupling stiffness matrices from the laminated plate theory as

$$(A_{11}, B_{11}, D_{11}) = \int_{-h/2}^{h/2} Q_{11}^{(i)}[1, z, z^2]\,\mathrm{d}z \tag{8}$$

$$A_{55} = \int_{-h/2}^{h/2} Q_{55}^{(i)}\,\mathrm{d}z \tag{9}$$

$Q_{11}^{(i)}$ and $Q_{55}^{(i)}$ represent the normal and transverse shear stiffnesses, respectively, of the ith ply.

2. Adherend Portion 5

Because of the small length-to-thickness ratio of adherend portion 5, which is a single ply, displacement distributions u and w in the x and z directions, respectively, are assumed to follow the "semi-elastic medium" approach. The normal and shear stress resultants N_{5x} and Q_{5z}, and the bending moment M_{5y} per unit width are related to the strains within the adherend portion and the constitutive relations of the adhesive material. Because adherend portion 5 is only one ply and very thin, the normal strain and slope at the midplane, $\mathrm{d}u_5^o/\mathrm{d}x$ and $\mathrm{d}w_5^o/\mathrm{d}x$, are used to determine N_{5x} and Q_{5z}. Also, because of the small thickness, M_{5y} is assumed to be negligible:

$$N_{5x} = \int_{-h_2/2}^{h_2/2} Q_{11}\frac{\mathrm{d}u_5^o(x)}{\mathrm{d}x}\,\mathrm{d}z \tag{10}$$

$$M_{5y} = \int_{-h_2/2}^{h_2/2} Q_{11}\frac{\mathrm{d}u_5^o(x)}{\mathrm{d}x} z\,\mathrm{d}z \approx 0 \tag{11}$$

$$Q_{5z} = \int_{-h_2/2}^{h_2/2} k_s Q_{55}\left[\frac{\mathrm{d}u_5^o(x)}{\mathrm{d}z} + \frac{\mathrm{d}w_5^o(x)}{\mathrm{d}x}\right]\mathrm{d}z \tag{12}$$

To correlate the shear and peel stresses at the adherend/adhesive interface at the bottom of adherend portion 5, the displacements at the midplane and bottom surface of adherend portion 5 are used, assuming that σ_z and τ_{xz} are uniform within the lower half of adherend portion 5. Therefore, as shown in Fig. 3, the shear stress and peel stresses τ_a^* and q_a^* are the same as σ_z and τ_{xz} within the lower half of adherend portion 5 and can be represented in terms of the midplane displacements u_5^o and w_5^o and the bottom surface displacements u_5^* and w_5^* as

$$\tau_a^* = \tau_{xz}|_{z=-h_2/2} = -G_{xz}\left[\frac{2}{h_2}(u_5^o - u_5^*) + \frac{\mathrm{d}w_5^o}{\mathrm{d}x}\right] \tag{13}$$

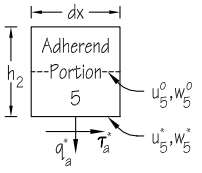

Fig. 3 Free-body diagram of adherend portion 5.

$$q_a^* = \sigma_z|_{z=-h_2/2} = \left(\frac{\upsilon_{xz} + \nu_{xy}\upsilon_{yz}}{E_x E_y \Delta}\right)\frac{\mathrm{d}u_5^o}{\mathrm{d}x} + 2\left(\frac{1 - \upsilon_{xy}\upsilon_{yx}}{E_x E_y \Delta}\right)\frac{(w_5^o - w_5^*)}{h_2} \tag{14}$$

where h_2 is the thickness of one single ply, υ_{xy} and υ_{yx} are Poisson's ratios in the x–y plane, υ_{xz} is Poisson's ratio in the x–z plane, υ_{yz} is Poisson's ratio in the y–z plane, and E_x, E_y, and G_{xz} are the moduli of elasticity in the x and y directions and shear modulus in the x–z plane, respectively. Δ can be given as

$$\Delta = \frac{1 - \upsilon_{xy}\upsilon_{yx} - \upsilon_{yz}\upsilon_{zy} - \upsilon_{zx}\upsilon_{xz} - 2\upsilon_{xy}\upsilon_{yz}\upsilon_{zx}}{E_x E_y E_z} \tag{15}$$

where υ_{zy} is Poisson's ratio in the z–y plane, υ_{zx} is Poisson's ratio in the x–z plane, and E_z is the modulus of elasticity in the z direction.

3. Adherend Portion 8

Similar to adherend portion 5, adherend portion 8 is also a single ply. The semi-elastic medium approach is considered for adherend portion 8 as well. The normal and shear stress resultant and bending moment per unit width can be related to the displacement fields as specified in Eqs. (10–12). The shear and peel stresses at the bottom surface of adherend portion 8 are formulated using the same methodology used for adherend portion 5, Eqs. (13) and (14), in terms of the midplane displacements u_8^o and w_8^o and the bottom surface displacements u_8^* and w_8^*.

The shear and peel stresses τ_i and σ_i at the upper surface of adherend portion 8, as shown in Fig. 4, which are the interlaminar stresses between adherend portions 7 and 8, are to be used for the equivalent crack-tip forces calculation and, later on, for the strain-energy release rate determination. Assuming uniform σ_z and τ_{xz} within the upper half of adherend portion 8 and a perfect bond between adherend portions 7 and 8, based on the kinematics and constitutive relations, τ_i and σ_i are related to the displacement functions of adherend portions 7 and 8 as

$$q_i = \left(\frac{\upsilon_{xz} + \nu_{xy}\upsilon_{yz}}{E_x E_y \Delta}\right)\frac{1}{2}\frac{\mathrm{d}}{\mathrm{d}x}\left(u_7^o - \frac{h_1}{2}\psi_7 + u_8^o\right) + \left(\frac{1 - \upsilon_{xy}\upsilon_{yx}}{E_x E_y \Delta}\right)\left[\frac{2}{h_2}\left(u_7^o - \frac{h_1}{2}\psi_7 - u_8^o\right) + \frac{\mathrm{d}w_8^o}{\mathrm{d}x}\right] \tag{16}$$

$$\tau_i = -G_{xz}\left[\frac{2}{h_2}\left(u_7^o - \frac{h_1}{2}\psi_7 - u_8^o\right) + \frac{\mathrm{d}w_8^o}{\mathrm{d}x}\right] \tag{17}$$

The shear and peel stresses τ_a^* and q_a^* at the bottom surface of adherend portion 8 are derived in the same way as those in adherend portion 5, and u_8^* and w_8^* shown in Fig. 4 will be solved later by equating the corresponding adhesive stress distributions given by the kinematics of adherend portions 8 and 9.

B. Adhesive Formulation

The adhesive is assumed to behave as an elastic-isotropic material. Using the kinematics of the adherends and assuming a perfect bond between the adhesive and the adherend surfaces, the adhesive strains are related to the displacements of the surfaces of the adherend portions adjacent to the adhesive. According to the discretized model shown in Fig. 2, an adhesive bond line is present in regions 1, 3, 4, and 6. The general formulas for regions 1 and 6 are the same where the upper and lower adherends contain only one adherend portion. In regions 3 and 4, however, the adherend above the adhesive is modeled as two adherend portions. Therefore, the adhesive formulation in regions 3 and 4 are different than those in regions 1 and 6.

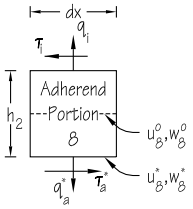

Fig. 4 Free-body diagram of adherend portion 8.

1. Adhesive Formulation in Regions 1 and 6

In terms of the displacement field of the upper and lower adherends, the adhesive strains in regions 1 and 6, with traditional sign conventions, can be written as

$$\gamma_{xz} = \frac{1}{\eta}\left[(u^{oU} - u^{oL}) - \left(\frac{h^U}{2}\psi^U + \frac{h^L}{2}\psi^L\right)\right] + \frac{1}{2}\left(\frac{\mathrm{d}w^L}{\mathrm{d}x} + \frac{\mathrm{d}w^U}{\mathrm{d}x}\right) \tag{18}$$

$$\varepsilon_x = \frac{1}{2}\frac{\mathrm{d}}{\mathrm{d}x}\left[(u^{oL} + u^{oL}) + \left(\frac{h^L}{2}\psi^L - \frac{h^U}{2}\psi^U\right)\right] \tag{19}$$

$$\varepsilon_z = \frac{1}{\eta}(w^U - w^L) \tag{20}$$

where η is the adhesive thickness, and h^U and h^L are the thicknesses of the upper and lower adherends, respectively. Assuming a plane-strain condition, adhesive shear stress τ_a and peel stress q_a can be obtained as

$$q_a = \frac{E_a}{(1 + \nu_a)(1 - 2\nu_a)}[\nu\varepsilon_x + (1 - \nu_a)\varepsilon_z] \tag{21}$$

$$\tau_a = -G_a\gamma_{xz} \tag{22}$$

where the sign conventions are shown in Fig. 5, E_a is the Young's modulus, υ_a is the Poisson's ratio, and G_a is the shear modulus of the adhesive.

2. Adhesive Formulation in Regions 3 and 4

In regions 3 and 4, the adherend portions above the adhesive, namely, adherend portion 5 in region 3 and adherend portion 8 in region 4, are a single ply. While the adherend portion above the adhesive is modeled using the semi-elastic media approach, the adherend portion below the adhesive is modeled using the first-order laminated plate theory. In terms of the displacement fields of the adherend portions above and below the adhesive, the adhesive strains for regions 3 and 4 with the traditional sign conventions can be written as

$$\gamma_{xz} = \frac{1}{\eta}\left(u^* - u^{oL} - \frac{h^L}{2}\psi^L\right) + \frac{1}{2}\left(\frac{\mathrm{d}w^o}{\mathrm{d}x} + \frac{\mathrm{d}w^L}{\mathrm{d}x}\right) \tag{23}$$

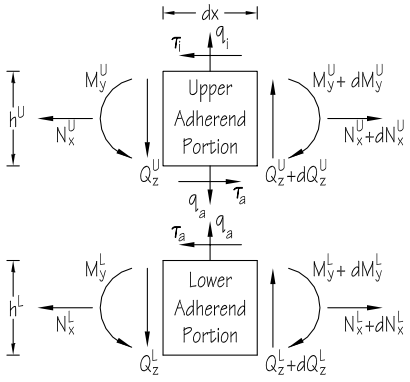

Fig. 5 General free-body diagram and sign convention.

$$\varepsilon_x = \frac{1}{2}\left(\frac{\mathrm{d}u^*}{\mathrm{d}x} + \frac{\mathrm{d}[u^{oL} + (h^L/2)\psi^L]}{\mathrm{d}x}\right) \tag{24}$$

$$\varepsilon_z = \frac{1}{\eta}(w^* - w^L) \tag{25}$$

where u^* and w^* are the displacements in the x and z directions, respectively, at the bottom surface of the adherend portion immediately above the adhesive, as shown in Figs. 3 and 4. The adhesive shear stress τ_a and peel stresses q_a can be obtained by substituting Eqs. (23–25) into Eqs. (21) and (22).

C. Adherend Equilibrium Equations

To establish the equations of equilibrium for each adherend portion, a free-body diagram of a differential element from the overlap regions is illustrated in Fig. 5. The upper adherend portion shown in the figure is the adherend portion immediately above the adhesive and represents adherend portions 1, 5, 8, and 12 in regions 1, 3, 4, and 6, respectively. The lower adherend portion in the figure is the lower adherend under the adhesive in each region. The general equations for force and moment equilibrium of the adherend portion above the adhesive are given as

$$\frac{\mathrm{d}N_x^U}{\mathrm{d}x} = \tau_i - \tau_a \tag{26}$$

$$\frac{\mathrm{d}M_y^U}{\mathrm{d}x} = Q_z^U + \frac{h^U}{2}(\tau_a + \tau_i) \tag{27}$$

$$\frac{\mathrm{d}Q_z^U}{\mathrm{d}x} = q_a - q_i \tag{28}$$

As mentioned previously, τ_a and q_a are the shear and peel stresses of the adhesive, whereas τ_i and q_i are the interlaminar shear and peel stresses, respectively, and h^U is the thickness of the upper adherend portion. It should be noted that τ_i and q_i do not exist in regions 1 and 6 because the upper adherend portions in these two regions are modeled as one piece, while the upper adherend portions in regions 3 and 4 are one ply, and τ_i and q_i are the interlaminar stresses, as shown in Figs. 3 and 4.

Three equilibrium equations can also be obtained for the adherend portion below the adhesive in a similar manner, but without any stresses at the bottom surface, as

$$\frac{\mathrm{d}N_x^L}{\mathrm{d}x} = \tau_a \tag{29}$$

$$\frac{\mathrm{d}M_y^L}{\mathrm{d}x} = Q_z^L + \frac{h^L}{2}\tau_a \tag{30}$$

$$\frac{\mathrm{d}Q_z^L}{\mathrm{d}x} = -q_a \tag{31}$$

where h^L is the thickness of the adherend portion below the adhesive.

Based on the general equilibrium equations for the adherend portions above and below the adhesive, equations of equilibrium for each adherend portion can be written and are described in detail next.

1. Region 1: Portions 1 and 2

From the free-body diagram in Fig. 5, it can be observed that $\tau_i = 0$ and $q_i = 0$, because the top surface of adherend portion 1 is a free-traction surface. Hence, Eqs. (26–31) can be rewritten as

$$\frac{\mathrm{d}N_{1x}}{\mathrm{d}x} = -\tau_a \tag{32}$$

$$\frac{\mathrm{d}M_{1y}}{\mathrm{d}x} = Q_{1z} + \frac{h}{2}\tau_a \tag{33}$$

$$\frac{\mathrm{d}Q_{1z}}{\mathrm{d}x} = q_a \tag{34}$$

$$\frac{\mathrm{d}N_{2x}}{\mathrm{d}x} = \tau_a \tag{35}$$

$$\frac{\mathrm{d}M_{2y}}{\mathrm{d}x} = Q_{2z} + \frac{h}{2}\tau_a \tag{36}$$

$$\frac{\mathrm{d}Q_{2z}}{\mathrm{d}x} = -q_a \tag{37}$$

By substituting the stress resultants from Eqs. (5–7) and the adhesive stresses τ_a and q_a from Eqs. (21) and (22) and Eqs. (18–20) into Eqs. (32–37), six coupled second-order ordinary differential equations in terms of u_1^o, u_2^o, ψ_1, ψ_2, w_1, and w_2 are obtained.

2. Region 2: Adherend Portion 3

Region 2 represents a notch in the overall specimen geometry. Because of the interlaminar failure assumed between adherend portions 4 and 5, where the first ply is supposed to continue from the lower right end of adherend portion 3 and form adherend portion 5, a crack is initiated between adherend portions 3 and 5, as shown in Fig. 6, as the "free surface." Because of the free surface at the lower right end of adherend portion 3, the effective thickness and the tensile, bending, and shear stiffness of adherend portion 3 are different from its left end to its right end. Based on the free-body diagram shown in Fig. 6, equations of equilibrium can be written as

$$N_{3x}^L = N_{3x}^R \tag{38}$$

$$Q_{3z}^L = Q_{3z}^R \tag{39}$$

$$M_{3y}^R = M_{3y}^L - N_{3x}^L\frac{h_2}{2} + Q_{3z}^L L_2 \tag{40}$$

where superscripts L and R refer to the left and right ends of adherend portion 3, respectively, h_2 is the thickness of a single ply, and L_2 is the entire length of adherend portion 3.

To obtain u_3^o, ψ_3, and w_3 at the right end of adherend portion 3, the following equations are used, assuming a small change in their derivatives:

$$u_3^o|_{x_2=L_2} = u_3^o|_{x_2=0} + \frac{L_2}{2}\left(\left.\frac{\mathrm{d}u_3^o}{\mathrm{d}x}\right|_{x_2=0} + \left.\frac{\mathrm{d}u_3^o}{\mathrm{d}x}\right|_{x_2=L_2}\right) \tag{41}$$

$$\psi_3|_{x_2=L_2} = \psi_3|_{x_2=0} + \frac{L_2}{2}\left(\left.\frac{\mathrm{d}\psi_3}{\mathrm{d}x}\right|_{x_2=0} + \left.\frac{\mathrm{d}\psi_3}{\mathrm{d}x}\right|_{x_2=L_2}\right) \tag{42}$$

$$w_3|_{x_2=L_2} = w_3|_{x_2=0} + \frac{L_2}{2}\left(\left.\frac{\mathrm{d}w_3}{\mathrm{d}x}\right|_{x_2=0} + \left.\frac{\mathrm{d}w_3}{\mathrm{d}x}\right|_{x_2=L_2}\right) \tag{43}$$

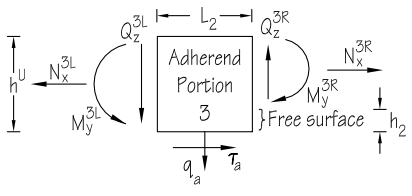

Fig. 6 Free-body diagram of adherend portion 3.

where the first-order derivatives of u_3^o, ψ_3, and w_3 are at the right end, where $x_2 = L_2$ can be determined by the following equations, which are based on equilibrium equations (38–40). In the following equations, (44–46), the values of u_3^o, ψ_3, w_3 and their derivatives at the left end, where $x_2 = 0$, are obtained from the right end of adherend portion 1 using the continuity condition. It should be noted that the stiffnesses A_{11}, B_{11}, D_{11}, and A_{55} have different values at the left and right ends due to delamination of the first ply at the right end:

$$\left(A_{11}\frac{\mathrm{d}u_3^o}{\mathrm{d}x}\right)\Big|_{x_2=0}+\left(B_{11}\frac{\mathrm{d}\psi_3}{\mathrm{d}x}\right)\Big|_{x_2=0}=\left(A_{11}\frac{\mathrm{d}u_3^o}{\mathrm{d}x}\right)\Big|_{x_2=L_2}+\left(B_{11}\frac{\mathrm{d}\psi_3}{\mathrm{d}x}\right)\Big|_{x_2=L_2} \tag{44}$$

$$\left[k_sA_{55}\left(\psi_3+\frac{\mathrm{d}w_3}{\mathrm{d}x}\right)\right]\Big|_{x_2=0}=\left[k_sA_{55}\left(\psi_3+\frac{\mathrm{d}w_3}{\mathrm{d}x}\right)\right]\Big|_{x_2=L_2} \tag{45}$$

$$\begin{aligned}&\left(B_{11}\frac{\mathrm{d}u_3^o}{\mathrm{d}x}\right)\Big|_{x_2=L_2}+\left(D_{11}\frac{\mathrm{d}\psi_3}{\mathrm{d}x}\right)\Big|_{x_2=L_2}\\&=\left(B_{11}\frac{\mathrm{d}u_3^o}{\mathrm{d}x}\right)\Big|_{x_2=0}+\left(D_{11}\frac{\mathrm{d}\psi_3}{\mathrm{d}x}\right)\Big|_{x_2=0}-\frac{h_2}{2}\left[\left(A_{11}\frac{\mathrm{d}u_3^o}{\mathrm{d}x}\right)\Big|_{x_2=0}\right.\\&\left.+\left(B_{11}\frac{\mathrm{d}\psi_3}{\mathrm{d}x}\right)\Big|_{x_2=0}\right]+L_2\left[k_sA_{55}\left(\psi_3+\frac{\mathrm{d}w_3}{\mathrm{d}x}\right)\right]\Big|_{x_2=0}\end{aligned} \tag{46}$$

3. Region 3: Adherend Portion 4

Because of first-ply failure at the bottom surface and the free-traction surface at the top, equations of equilibrium of adherend portion 4 can be written as

$$\frac{\mathrm{d}N_{4x}}{\mathrm{d}x}=0 \tag{47}$$

$$\frac{\mathrm{d}M_{4y}}{\mathrm{d}x}=Q_{4z} \tag{48}$$

$$\frac{Q_{4z}}{dx}=0 \tag{49}$$

Substituting the stress resultants as functions u_4^o, ψ_4, and w_4 yields three coupled second-order ordinary differential equations in terms of u_4^o, ψ_4, and w_4.

4. Region 3: Adherend Portions 5 and 6

As previously noted, adherend portion 5 contains a single ply and is separated from adherend portion 4 due to the prescribed interlaminar crack. The equations of equilibrium of adherend portions 5 and 6 are similar to those for adherend portions 1 and 2 but without considering the bending moment in adherend portion 5, as previously mentioned,

$$\frac{\mathrm{d}N_{5x}}{\mathrm{d}x}=-\tau_a \tag{50}$$

$$\frac{\mathrm{d}Q_{5z}}{\mathrm{d}x}=q_a \tag{51}$$

$$\frac{\mathrm{d}N_{6x}}{\mathrm{d}x}=\tau_a \tag{52}$$

$$\frac{\mathrm{d}M_{6y}}{\mathrm{d}x}=Q_{6z}+\frac{h}{2}\tau_a \tag{53}$$

$$\frac{\mathrm{d}Q_{6z}}{\mathrm{d}x}=-q_a \tag{54}$$

Plugging in the stress resultants from Eqs. (10) and (12) for N_{5x} and Q_{5z}, Eqs. (5–7) for N_{6x}, M_{6y}, and Q_{6z}, five coupled second-order ordinary differential equations u_5^o, w_5^o, u_6^o, w_6, and ψ_6 are obtained. Thus, u_5^* and w_5^* can be solved in terms of all other variables by equating the shear and peel stresses at the bottom surface of adherend portion 5, as specified in Eqs. (13) and (14), with the adhesive shear and peel stresses using adhesive strains in Eqs. (23–25) as

$$\tau_a^*=\tau_a \tag{55}$$

$$q_a^*=q_a \tag{56}$$

5. Region 4: Adherend Portions 7, 8, and 9

A similar approach as that used for region 3 for adherend portions 5 and 6 can be applied to region 4, with an additional adherend portion at the top and at the interlaminar stresses. Eight equations can be written based on normal stress resultants, bending moment, and shear stress resultants as

$$\frac{\mathrm{d}N_{7x}}{\mathrm{d}x}=-\tau_i \tag{57}$$

$$\frac{\mathrm{d}M_{7y}}{\mathrm{d}x}=Q_{7z}+\frac{h_1}{2}\tau_i \tag{58}$$

$$\frac{\mathrm{d}Q_{7z}}{\mathrm{d}x}=q_i \tag{59}$$

$$\frac{\mathrm{d}N_{8x}}{\mathrm{d}x}=\tau_a-\tau_i \tag{60}$$

$$\frac{\mathrm{d}Q_{8z}}{\mathrm{d}x}=q_i-q_a \tag{61}$$

$$\frac{\mathrm{d}N_{9x}}{\mathrm{d}x}=\tau_a \tag{62}$$

$$\frac{\mathrm{d}M_{9y}}{\mathrm{d}x}=Q_{9z}+\frac{h}{2}\tau_a \tag{63}$$

$$\frac{\mathrm{d}Q_{9z}}{\mathrm{d}x}=-q_a \tag{64}$$

where h_1 and h are thicknesses of adherend portions 7 and 9, respectively. The interlaminar shear and peel stresses τ_i and q_i between adherend portions 7 and 8 are in terms of displacement fields of adherend portions 7 and 8, as shown in Eqs. (16) and (17).

Using the same methodology as used in region 3, adherend portions 5 and 6 u_8^* and w_8^* can be determined by equating τ_a^* and q_a^* with τ_a and q_a.

6. Region 5: Adherend Portion 10

This region represents a notch in the model. Equations of equilibrium are the same as those given for adherend portion 4, while stiffness matrices are different.

7. Region 6: Adherend Portions 11 and 12

Because of the similarities between regions 1 and 6, the same equations of equilibrium can be driven for region 6 with new variables.

The overall system of governing equations, including all six regions, contains 31 second-order ordinary differential equations with 31 unknown variables. A total of 62 boundary conditions are obtained at the two ends of each region, based on either continuity or applied force conditions. The symbolic solver Maple 9.52 was used to solve the system of equations and obtain the displacement, strain, and stress fields.

III. Strain-Energy Release-Rate Calculation

Once the stress, strain, and displacement fields are known in the adhesive-bonded single-lap composite joints, the VCCT is applied to estimate the SERR of the joint with a prescribed crack. According to linear-elastic fracture mechanics, the energy released due to an extension/propagation (virtual crack extension) of a crack is equivalent to the work needed to close that extension/propagation [14] and this is the foundation of VCCT—a virtual crack closure technique.

Cracks usually start at locations of high stress concentration. For the ASTM D3165 specimen configuration shown in Fig. 1, the critical area is located at the lower part of the junction between adherend portions 3 and 4. Often times, it is either the adhesive/adherend interface below the junction that starts to fail, in the case of metal adherends, or the adherend that starts to fail at the junction, in the case of composite adherends. Failure of such joints at the adherend/adhesive interface with either thin or thick bond lines has been studied by Yang et al. [16,17]. Because the focus of this current study is on the first-ply failure of the adherend, the failure is assumed to initiate at the junction of adherend portions 3 and 4 and at the first ply from the adhesive. Thereafter, the crack propagates along the length direction of the joint until the entire joint unzips.

A. Analytical Approach

In deriving the expression for the SERR, a joint is assumed to have an overlap length l_o, a notch size L_2, and a crack length a, which is located at the interface of the first ply of the upper adherend, as shown in Fig. 7. The displacement of the crack tip C, after a load is applied, can be determined using the mechanical model previously described with an overlap region length of $L_4 = l_o - a$.

Interlaminar and adhesive stress distributions can be determined using the solution from the analytical model described previously. Before the crack growth of an additional small length b, as shown in Fig. 8, the first ply between C' and C adheres to the upper adherend where interlaminar shear and peel stresses exist at the interface, as shown on the left side of Fig. 9.

The interlaminar shear and peel stresses between C' and C vanish after the crack propagates a small length b. The equivalent crack-tip forces N_C, M_C, and Q_C, corresponding to a small crack propagation b, are related to the shear and peel stresses between C' and C, as shown on the right side of Fig. 9, and can be calculated as

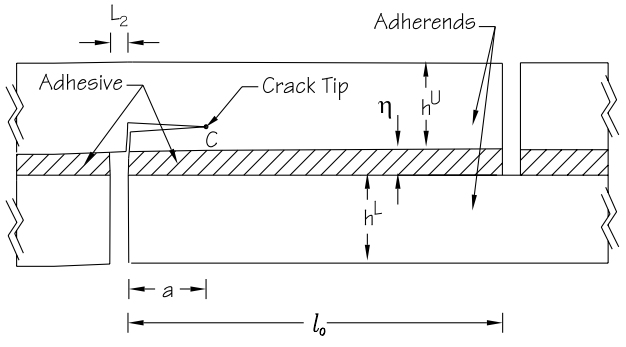

Fig. 7 ASTM D3165 specimen with initial crack of length *a*.

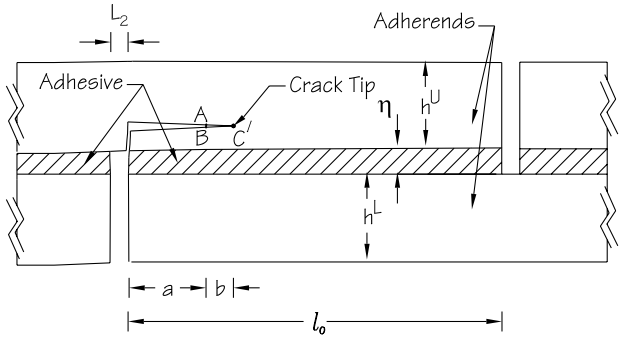

Fig. 8 ASTM D3165 specimen with a virtual crack extension of length *b*.

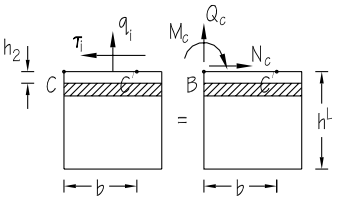

Fig. 9 Equivalent forces at the crack tip.

$$N_C = \int_0^b \tau_i \, \mathrm{d}x_4 \tag{65}$$

$$M_C = -\int_0^b q_i x_4 \, \mathrm{d}x_4 \tag{66}$$

$$Q_C = -\int_0^b q_i \, \mathrm{d}x_4 \tag{67}$$

where the interlaminar shear stress τ_i and peel stress q_i are obtained from the stress model with an overlap length $L_4 = l_o - a$. Note that only the first ply, adhesive layer, and lower adherend are shown in Fig. 9 and that the positive directions of N_C, M_C, and Q_C are defined to be consistent with the positive directions of displacements u, ψ, and w, respectively.

After the crack propagates a small length b, the previous crack tip C separates into two points A and B, as shown in Fig. 8. To determine the relative displacement between points A and B, a subsequent stress analysis is performed using a joint with a central overlap length $L_4 = l_o - a - b$, which simulates the overlap up to the new crack tip C'.

To close the virtual crack propagation (length b), crack-tip forces are applied on points A and B to move them back to the location of the original crack tip C. Therefore, the total work required to close the small crack propagation b is

$$W = \tfrac{1}{2}[N_C(u_B - u_A) + M_C(\psi_B - \psi_A) + Q_C(w_B - w_A)] \tag{68}$$

For joints with a unit width, the strain-energy release rate is defined as the derivative of energy released from the crack propagation with respect to the length of the crack propagation as

$$G_T = \frac{\mathrm{d}U}{\mathrm{d}a} \tag{69}$$

where U is the strain energy stored in the body. Based on the VCCT, the total energy released from the crack propagation is equivalent to the work needed to close the same crack propagation. With a virtual crack propagation of length b, the total strain-energy release rate G_T, which is a summation of the mode I strain-energy release rate G_I and the mode II strain-energy release rate G_{II}, can be calculated as

$$G_T = G_I + G_{II} = \frac{\mathrm{d}U}{\mathrm{d}a} \cong \frac{W}{b}$$
$$= \frac{1}{2b}[N_C(u_B - u_A) + M_C(\psi_B - \psi_A) + Q_C(w_B - w_A)] \tag{70}$$

B. Finite Element Approach Using VCCT

The strain-energy release rate due to the small increase in crack length is equivalent to the energy required to close that small crack increment. Therefore, the strain-energy release rate can be computed by finite element models using the VCCT [25,26]. As shown in Fig. 10, the tip of a crack with an original length a is located at C.

Assuming a virtual crack propagation of length b, the new crack tip becomes C', and the original crack tip becomes two separate nodes f and g. If nodes f and g are restrained at the original crack-tip location, this virtual crack of length b is closed, and the work to close this virtual crack can be calculated by multiplying the reaction forces at nodes f and g by the relative displacements of these two separate nodes to the original crack tip C. The procedures to calculate the SERR using finite element software are described as follows:

1) Build the finite element model with an original crack of length a, and determine the displacements of crack tip C, u_c, and w_c in the x and z directions, respectively.

2) Propagate the crack with a small length b (usually one element size); then the original crack tip C becomes two separate nodes. Record the displacements of both nodes u_f, w_f, u_g, and w_g.

3) Constrain the two separate nodes so that they have the same displacements as the original crack tip C, and obtain the reaction forces F_{xf}, F_{yf}, F_{xg}, and F_{yg}.

4) The work needed to close the virtual crack is

$$W = \tfrac{1}{2}[F_{xf}(u_c - u_f) + F_{yf}(w_c - w_f)] + \tfrac{1}{2}[F_{xg}(u_c - u_g) + F_{yg}(w_c - w_g)] \tag{71}$$

The total strain-energy release rate is then obtained by

$$G_T = \frac{W}{b} \tag{72}$$

ABAQUS has developed a VCCT subroutine called virtual crack closure for ABAQUS (VFA) [24], which calculates modes I, II, and III strain-energy release rates following a proper procedure. In the present study, two-dimensional four-node linear plane-strain quadrilateral elements were used in the finite element model for the VCCT application. There are seven elements through the adherend thickness corresponding to seven plies of E765/T300 3KPW plane weave graphite/epoxy with orientation and sequence of $[0/60/-60/0/-60/60/0]$.

C. Finite Element Approach Using *J* Integral

Finite element models with the J-integral calculation were constructed using ABAQUS [18] to verify the present analytical model. The J integral is usually used in quasi-static fracture analysis to characterize the energy release associated with crack propagation. It is equivalent to the strain-energy release rate if the material response is linear elastic. Considering an arbitrary counterclockwise path (Γ) around the crack tip, as illustrated in Fig. 11, the J integral is defined as

$$J = \int_\Gamma \left(w\,\mathrm{d}y - \sum_{i=1}^{3} T_i \frac{\partial u_i}{\partial x}\,\mathrm{d}s \right) \tag{73}$$

where w is the strain-energy density, u_1, u_2, and u_3 are the components of the displacement vector, $\mathrm{d}s$ is the incremental length along the contour Γ, and T_1, T_2, and T_3 are components of the traction vector. The traction is a stress vector normal to the contour. In other words, T_1, T_2, and T_3 are the normal stresses acting at the boundary if a free-body diagram on the material inside of the contour is constructed.

Several contour integral evaluations are possible at each location along the crack front. In a finite element model, each evaluation can be thought of as the virtual motion of a block of material surrounding the crack tip. Each block is defined by contours, and each contour is a ring of elements completely surrounding the crack tip or crack front from one crack face to the opposite crack face. These rings of elements are defined recursively to surround all previous contours. ABAQUS/Standard automatically finds the elements that form each ring from the node sets given as the crack-tip or crack-front definition. Each contour provides an evaluation of the contour integral [18].

Theoretically, the J integral should be independent of the domain used, but the J integral estimated from different rings may vary because of the approximate nature of the finite element solution. A strong variation in these estimates, commonly called domain dependent or contour dependent, indicates a need for mesh refinement (provided that the problem is suitable for contour integrals). Numerical tests suggest that the estimate from the first ring of elements abutting the crack front does not provide a high-accuracy result, so at least two contours are recommended. In the present study, five contours were calculated, and the average was taken as the final J-integral value. This method is quite robust in the sense that accurate contour integral estimates are usually obtained even with quite coarse meshes.

Sharp cracks, where the crack faces lie on top of one another in the undeformed configuration, are usually modeled using small-strain assumptions. Focused meshes for the J-integral calculation should normally be used for small-strain fracture-mechanics evaluations.

For linear-elastic materials, the linear-elastic fracture-mechanics approach predicts an $r^{-1/2}$ singularity near the crack tip, where r is the distance from the crack tip. In finite element analyses, forcing the elements at the crack tip to exhibit an $r^{-1/2}$ strain singularity greatly improves accuracy and reduces the need for a high degree of mesh refinement at the crack tip [27]. This $r^{-1/2}$ singularity can be produced using an eight-node quadrilateral element by moving the midside nodes to the quarter points, as noted by Barsoum [28] and Henshell and Shaw [29]. Yang et al. [16,17] have demonstrated a complete step-by-step procedure calculating the J integral using ABAQUS.

IV. Results and Discussion

In the present study, ASTM D3165 was modeled analytically to determine the strain-energy release rate using the methodology described previously. The symbolic solver Maple 9.52 was used as the mathematical tool. The finite element models for the VCCT and J integral were conducted using ABAQUS 6.5-1 to verify the analytical results.

To demonstrate the application of the developed model, E765/T300 3KPW plane weave (graphite/epoxy) with a ply thickness of 0.25 mm and a quasi-isotropic layup sequence of

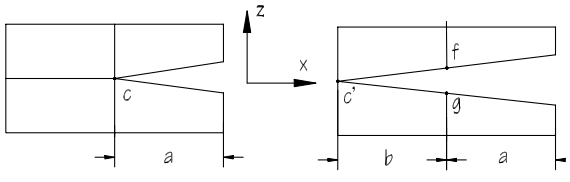

Fig. 10 Finite element approach using VCCT.

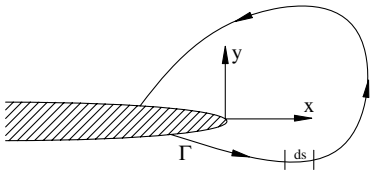

Fig. 11 Arbitrary contour around crack tip.

$[60/-60/0/-60/60/0]$ was used. The engineering constants were $E_{11} = 56.50$ GPa, $E_{22} = 55.20$ GPa, $G_{12} = 3.86$ GPa, and $v_{12} = 0.076$. For convenience, other mechanical properties of adherends were assumed as

$$E_{33} = 8.00 \text{ GPa}, \qquad G_{13} = G_{23} = 3.56 \text{ GPa}$$
$$v_{13} = v_{23} = 0.35$$

The shear correction factor $k_s = 5/6$ was assumed. Two different paste adhesives with distinct moduli, Hysol EA9394 and PTM&W ES6292, were used to fabricate the joint specimens and demonstrate the capabilities of the analytical model. Adhesives have the following material properties:

Hysol EA 9394	$E_a = 4.24$ GPa	$v_a = 0.45$
PTM&W ES 6292	$E_a = 1.58$ GPa	$v_a = 0.31$

The joint dimensions of the ASTM D3165 specimen include the central overlap length $l_o = 30$ mm, notch size $L_2 = 1.6$ mm, and adherend lengths outside the central overlap $L_1 = L_6 = 78.4$ mm. Based on the thin-adhesive assumption, three different thicknesses ($\eta = 0.051$ mm, 0.127 mm, and 0.203 mm) were considered in the investigation of the application of the analytical model.

Once the stress, strain, and displacement fields were obtained, the strain-energy release rates of the joints were estimated, and the solutions from the analytical models using the VCCT were compared with finite element models using the VCCT and finite element models using the J integral. Tensile load $P = 1.78$ kN was considered the minimum required failure load in the joint.

Numerical methods, such as finite element analysis, are usually mesh sensitive. A convergence test of finite element mesh size was conducted, and the results are shown in Fig. 12. The converged results were used to compare with the developed analytical model.

Figures 13 and 14 show the SERR comparison using the VCCT, the analytical model, and the J integral for different adhesives. From these figures, it can be seen that G_T increases with increased bond-line thickness; that is, the load-carrying capacity of the joint is lower for thicker adhesive if G_T is critical for joint failure. Discrepancy between the analytical model and the FE models occurs for thicker bond lines. This is because the current model assumes a thin bond line and the adhesive stresses are assumed uniform through the bond-line thickness. As shown in Figs. 15 and 16, G_I increases with adhesive thickness, whereas G_{II} decreases; in fact, both values compensate each other for higher values of G_T, as shown Fig. 13. The same trend can be observed in Figs. 17 and 18 for PTM&W ES 6292.

The strain-energy release rates for three different crack lengths ($a = 1.27$ mm, 1.91 mm, and 2.54 mm) are shown in Figs. 19 and 20. It can be seen that G_T decreases with increased crack length which shows the effect of crack arrest; that is, the crack would not propagate unless the load increases. If the failure criterion is set to be G_T and because G_T decreases with longer crack length, a stable crack growth can be expected. Figures 21 and 22 show variations of modes I and II for Hysol EA 9394. It can be concluded that either using mode I or mode II as the failure criterion, a stable crack growth is expected.

It can be seen that results from the finite element models with the VCCT and J integral are identical and show the same trend for thin adhesives, whereas the developed analytical model deviates about 10% from the finite element models. The deviation between finite element analysis and the analytical model comes from the assumption of the constant stresses through the thickness of the adhesive.

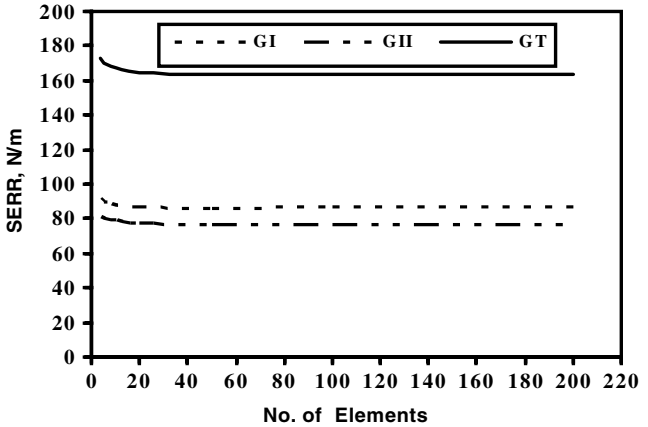

Fig. 12 Strain-energy release rate convergence of ASTM D3165 specimen versus number of elements for $\eta = 0.127$ mm, $a = 1.27$ mm, with Hysol EA 9394.

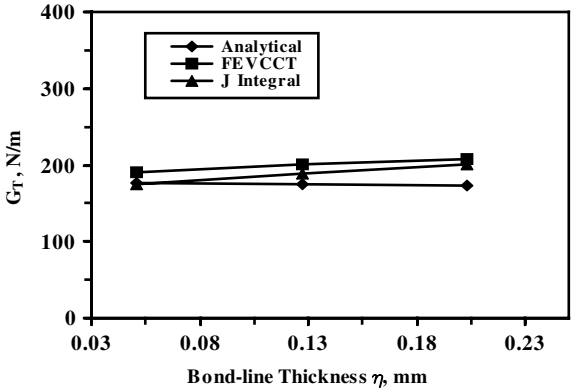

Fig. 13 Strain-energy release rate of ASTM D3165 specimen as a function of bond-line thickness for $a = 1.27$ mm with Hysol EA 9394 adhesive.

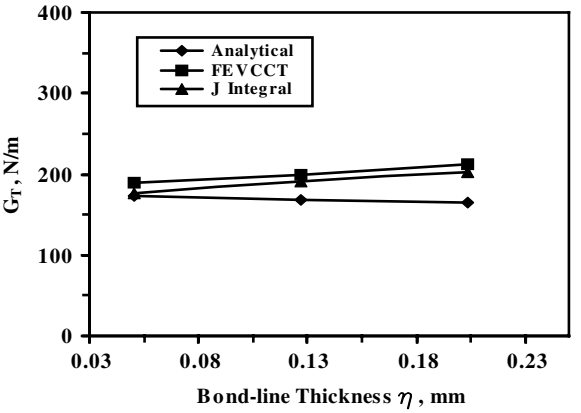

Fig. 14 Strain-energy release rate of ASTM D3165 specimen as a function of bond-line thickness for $a = 1.27$ mm with PTM&W ES 6292 adhesive.

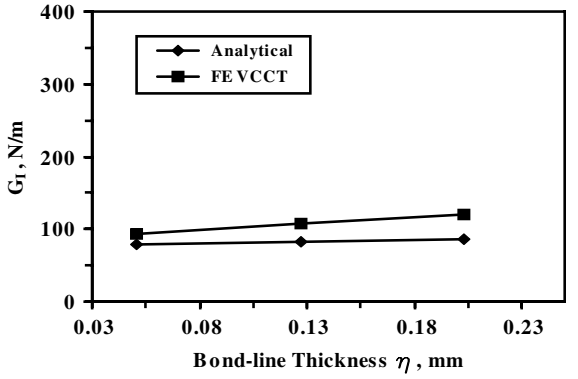

Fig. 15 Mode I strain-energy release rate of ASTM D3165 specimen as a function of bond-line thickness for $a = 1.27$ mm with Hysol EA 9394.

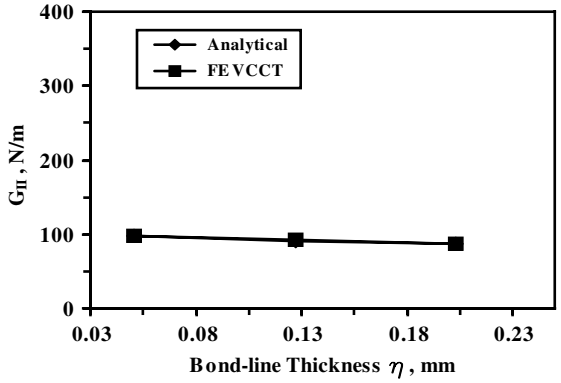

Fig. 16 Mode II strain-energy release rate of ASTM D3165 specimen as a function of bond-line thickness for $a = 1.27$ mm with Hysol EA 9394.

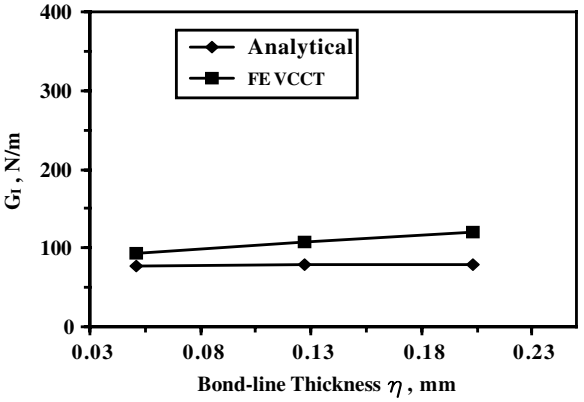

Fig. 17 Mode I strain-energy release rate of ASTM D3165 specimen as a function of bond-line thickness for $a = 1.27$ mm with PTM&W ES 6292.

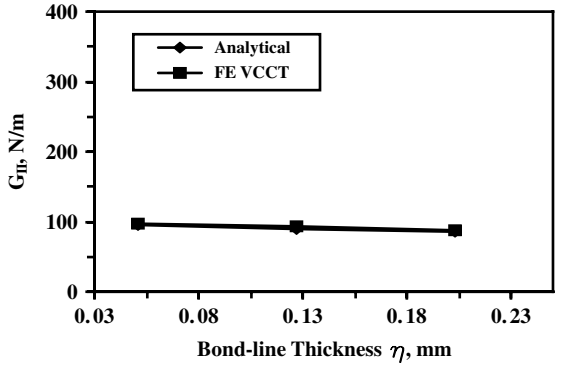

Fig. 18 Mode II strain-energy release rate of ASTM D3165 specimen as a function of bond-line thickness for $a = 1.27$ mm with PTM&W ES 6292.

V. Conclusions

An analytical method was developed to calculate the strain-energy release rate based on ASTM D3165 specimen geometry with a prescribed interlaminar crack. The stress and displacement fields for the adhesive-bonded single-lap composite joint were determined based on the laminated anisotropic plate theory. The virtual crack closure technique was applied effectively in conjunction with the analytical stress and displacement models in determining the strain-energy release rate. Results obtained from the developed analytical method correlated properly with results from the finite element models using both the VCCT and *J* integral. Therefore, the present study has given a description of a reasonably accurate, rapid-solution

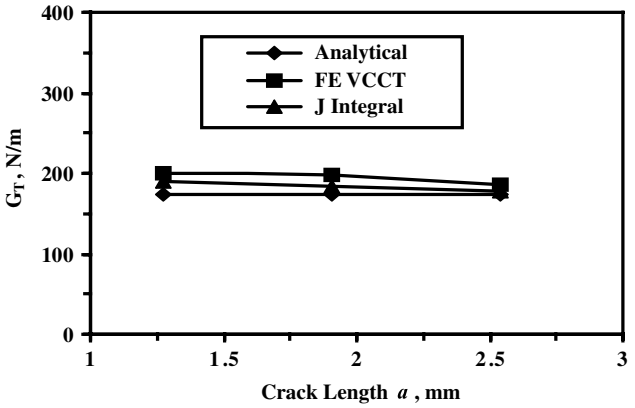

Fig. 19 Strain-energy release rate of ASTM D3165 specimen as a function of initial crack length for $\eta = 0.127$ mm with Hysol EA 9394.

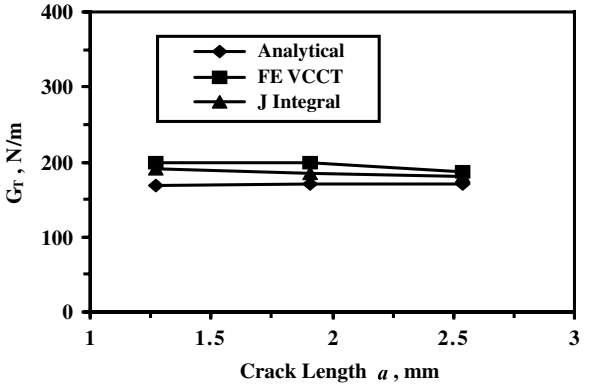

Fig. 20 Strain-energy release rate of ASTM D3165 specimen as a function of initial crack length for $\eta = 0.127$ mm with PTM&W ES 6292.

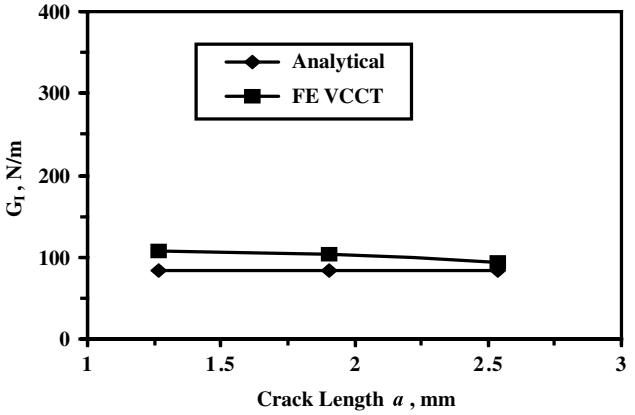

Fig. 21 Mode I strain-energy release rate of ASTM D3165 specimen as a function of initial crack length for $\eta = 0.127$ mm with Hysol EA 9394.

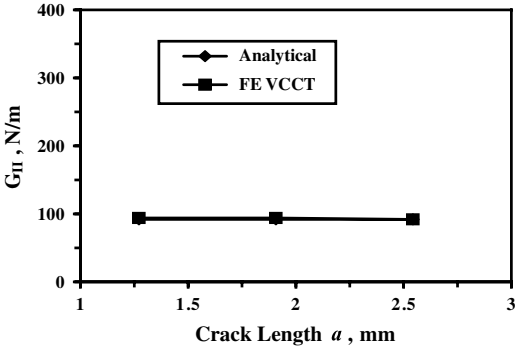

Fig. 22 Mode II strain-energy release rate of ASTM D3165 specimen as a function of initial crack length for $\eta = 0.127$ mm with Hysol EA 9394.

method for calculating the SERR of an adhesive-bonded single-lap composite joint.

Appendix: Boundary Conditions

Region 1:

$$u_1^o|_{x_1=0} = 0 \tag{A1}$$

$$w_1|_{x_1=0} = 0 \tag{A2}$$

$$M_{1y}|_{x_1=0} = 0 \tag{A3}$$

$$N_{1x}|_{x_1=0} = \frac{A_{11}^U}{A_{11}^U + A_{11}^L + E_a\eta} P \tag{A4}$$

$$M_{2y}|_{x_1=0} = 0 \tag{A5}$$

$$Q_{2z}|_{x_1=0} = 0 \tag{A6}$$

$$N_{2x}|_{x_1=L_1} = 0 \tag{A7}$$

$$M_{2y}|_{x_1=L_1} = 0 \tag{A8}$$

$$Q_{2z}|_{x_1=L_1} = 0 \tag{A9}$$

Region 3:

$$u_3^o|_{x_2=L_2} = u_4^o|_{x_3=0} \tag{A10}$$

$$w_3|_{x_2=L_2} = w_4|_{x_3=0} \tag{A11}$$

$$\psi_3|_{x_2=L_2} = \psi_4|_{x_3=0} \tag{A12}$$

$$N_{3x}|_{x_2=L_2} = N_{4x}|_{x_3=0} \tag{A13}$$

$$M_{3y}|_{x_2=L_2} = M_{4y}|_{x_3=0} \tag{A14}$$

$$Q_{3z}|_{x_2=L_2} = Q_{4z}|_{x_3=0} \tag{A15}$$

$$N_{5x}|_{x_3=0} = 0 \tag{A16}$$

$$M_{5y}|_{x_3=0} = 0 \tag{A17}$$

$$Q_{5z}|_{x_3=0} = 0 \tag{A18}$$

$$N_{6x}|_{x_3=0} = 0 \tag{A19}$$

$$M_{6y}|_{x_3=0} = 0 \tag{A20}$$

$$Q_{6z}|_{x_3=0} = 0 \tag{A21}$$

$$u_4^o|_{x_3=L_3} = u_7^o|_{x_4=0} \tag{A22}$$

$$w_4|_{x_3=L_3} = w_7|_{x_4=0} \tag{A23}$$

$$\psi_4|_{x_3=L_3} = \psi_7|_{x_4=0} \tag{A24}$$

$$N_{4x}|_{x_3=L_3} = N_{7x}|_{x_4=0} \tag{A25}$$

$$M_{4y}|_{x_3=L_3} = M_{7y}|_{x_4=0} \tag{A26}$$

$$Q_{4z}|_{x_3=L_3} = Q_{7z}|_{x_4=0} \tag{A27}$$

$$u_5^o|_{x_3=L_3} = u_8^o|_{x_4=0} \tag{A28}$$

$$w_5|_{x_3=L_3} = w_8|_{x_4=0} \tag{A29}$$

$$N_{5x}|_{x_3=L_3} = N_{8x}|_{x_4=0} \tag{A30}$$

$$Q_{5z}|_{x_3=L_3} = Q_{8z}|_{x_4=0} \tag{A31}$$

$$u_6^o|_{x_3=L_3} = u_9^o|_{x_4=0} \tag{A32}$$

$$w_6|_{x_3=L_3} = w_9|_{x_4=0} \tag{A33}$$

$$\psi_6|_{x_3=L_3} = \psi_9|_{x_4=0} \tag{A34}$$

$$N_{6x}|_{x_3=L_3} = N_{9x}|_{x_4=0} \tag{A35}$$

$$M_{6y}|_{x_2=L_3} = M_{9y}|_{x_4=0} \tag{A36}$$

Region 4:

$$N_{7x}|_{x_4=L_4} = 0 \tag{A37}$$

$$M_{7y}|_{x_4=L_4} = 0 \tag{A38}$$

$$Q_{7z}|_{x_4=L_4} = 0 \tag{A39}$$

$$N_{8x}|_{x_4=L_4} = 0 \tag{A40}$$

$$Q_{8z}|_{x_4=L_4} = 0 \tag{A41}$$

$$u_9^o|_{x_4=L_4} = u_{10}^o|_{x_5=0} \tag{A42}$$

$$w_9|_{x_4=L_4} = w_{10}|_{x_5=0} \tag{A43}$$

$$\psi_9|_{x_4=L_4} = \psi_{10}|_{x_5=0} \tag{A44}$$

$$N_{9x}|_{x_4=L_4} = N_{10x}|_{x_5=0} \tag{A45}$$

$$M_{9y}|_{x_4=L_4} = M_{10y}|_{x_5=0} \tag{A46}$$

$$Q_{9z}|_{x_4=L_4} = Q_{10z}|_{x_5=0} \tag{A47}$$

Region 5:

$$u_{10}^o|_{x_5=L_5} = u_{12}^o|_{x_6=0} \tag{A48}$$

$$w_{10}|_{x_5=L_5} = w_{12}|_{x_6=0} \tag{A49}$$

$$\psi_{10}|_{x_5=L_5} = \psi_{12}|_{x_6=0} \tag{A50}$$

$$N_{10x}|_{x_5=L_5} = N_{12x}|_{x_6=0} \tag{A51}$$

$$M_{10y}|_{x_5=L_5} = M_{12y}|_{x_6=0} \tag{A52}$$

$$Q_{10z}|_{x_5=L_5} = Q_{12z}|_{x_6=0} \tag{A53}$$

Region 6:

$$N_{11x}|_{x_6=0} = 0 \tag{A54}$$

$$M_{11y}|_{x_6=0} = 0 \tag{A55}$$

$$Q_{11z}|_{x_6=0} = 0 \tag{A56}$$

$$N_{11x}|_{x_6=L_6} = \frac{A_{11}^U}{A_{11}^U + A_{11}^L + E_a\eta} P \tag{A57}$$

$$M_{11y}|_{x_6=L_6} = 0 \tag{A58}$$

$$Q_{11z}|_{x_6=L_6} = 0 \tag{A59}$$

$$N_{12x}|_{x_6=L_6} = \frac{A_{11}^L}{A_{11}^U + A_{11}^L + E_a\eta} P \tag{A60}$$

$$M_{12y}|_{x_6=L_6} = 0 \tag{A61}$$

$$Q_{12z}|_{x_6=L_6} = 0 \tag{A62}$$

References

[1] Armanios, E. A., "Analysis of Delamination Related Fracture Processes in Composites," Preliminary Final Report, NASA-CR-184603, 1988.

[2] Yang, C., Tomblin, J. S., and Guan, Z., "Analytical Modeling of ASTM Lap Shear Adhesive Specimens," Federal Aviation Administration TR DOT/FAA/AR-02/130, 2003.

[3] Kutscha, D., "Mechanics of Adhesive-Bonded Lap-Type Joints: Survey and Review," U.S. Air Force TR AFML-TDR-64-298, 1964.

[4] Kutscha, D., and Hofer, K. E., Jr., "Feasibility of Joining Advanced Composite Flight Vehicles," U.S. Air Force TR AFML-TR-68-391, 1969.

[5] Matthews, F. L., Kilty, P. F., and Goodwin, E. W., "A Review of the Strength of Joints in Fiber-Reinforced Plastics: Part 2 Adhesively Bonded Joints," *Composites*, Vol. 13, No. 1, 1980, pp. 29–37.

[6] Vinson, J. R., "Adhesive Bonding of Polymer Composites," *Polymer Engineering and Science*, Vol. 29, No. 19, 1989, pp. 1325–1331. doi:10.1002/pen.760291904

[7] Yang, C., and Pang, S. S., "Stress-Strain Analysis of Single-Lap Composite Joints under Tension," *Journal of Engineering Materials and Technology*, Vol. 118, No. 2, 1996, pp. 247–255. doi:10.1115/1.2804896

[8] Huang, H., Yang, C., Tomblin, J. S., and Harter, P., "Stress and Failure Analyses of Adhesive-Bonded Composite Joints Using ASTM D3165 Specimens," *Journal of Composites Technology and Research*, Vol. 24, No. 2, 2002, pp. 345–356.

[9] Yang, C., Huang, H., Tomblin, J. S., and Sun, W., "Elastic-Plastic Model of Adhesive-Bonded Single-Lap Composite Joints," *Journal of Composite Materials*, Vol. 38, No. 4, 2004, pp. 293–309. doi:10.1177/0021998304039268

[10] Krueger, D., "The Virtual Crack Closure Technique: History, Approach and Applications," Technical Report NASA-CR-2002-211628, ICASE Report 2002-10, 2002.

[11] Davidson, B. D., Yu, L., and Hu, H., "Delamination of Energy Release Rate and Mode Mix in Three-Dimensional Layered Structures Using Plate Theory," *International Journal of Fracture*, Vol. 105, No. 1, 2000, pp. 81–104. doi:10.1023/A:1007672131026

[12] Park, O., and Sankar, B. V., "Crack-Tip Force Method for Computing Energy Release Rate in Delaminated Plates," *Composite Structures*, Vol. 55, No. 4, 2002, pp. 429–434. doi:10.1016/S0263-8223(01)00170-2

[13] Kim, I.-G., and Kong, C.-D., "Generalized Theoretical Analysis Method for Free-Edge Delaminations in Composite Laminates," *Journal of Materials Science*, Vol. 37, No. 9, 2002, pp. 1875–1880. doi:10.1023/A:1014903518913

[14] Wang, J. T., Xue, D. Y., Sleight, D. W., and Housner, J. M., "Computation of Energy Release Rate for Cracked Composite Panels with Nonlinear Deformation," *Proceedings of the 36th IAA/ASME/ASCE/AHS/ASC Structures, Structural Dynamics & Materials Conference*, AIAA, Washington, D.C., 1995, AIAA-95-1463-CP, Pt. 4, pp. 2713–2727.

[15] Wei, Y., Yang, T., Wan, Z., and Du, X., "New VCCT and Its Application in Composite Delamination Analysis," *Chinese Journal of Computational Mechanics*, Vol. 17, No. 3, 2000, pp. 308–312.

[16] Yang, C., Sun, W., Tomblin, J. S., and Smeltzer, S. S., II, "A Semi-Analytical Method for Determining the Strain Energy Release Rate of Cracks in Adhesively Bonded Single-Lap Composite Joints," *Journal of Composite Materials*, Vol. 41, No. 13, 2007, pp. 1579–1602. doi:10.1177/0021998306069872

[17] Yang, C., Chadegani, A., and Tomblin, J. S., "Strain Energy Release Rate Determination of Prescribed Cracks in Adhesively Bonded Single-Lap Composite Joints with Thick Bondlines," *Composites. Part B, Engineering*, Vol. 39, No. 5, 2008, pp. 863–873.

[18] ABAQUS/CAE User Manual and VFA Package, Ver. 6.5–1, Hibbit, Karlsson & Sorensen Inc., Providence, RI, 2004–2005.

[19] Armanios, E. A., and Rehfield, L. W., "Sublaminate Analysis of Interlaminar Fracture in Composites: Part 1—Analytical Model," *Journal of Composites Technology and Research*, Vol. 11, No. 4, 1989, pp. 135–146.

[20] Armanios, E. A., and Rehfield, L. W., "Interlaminar Analysis of Laminated Composites Using a Sublaminate Approach," *Proceedings of the 27th AIAA/ASME/ASCE/AHS Structures, Structural Dynamics, and Materials Conference*, AIAA, New York, 1986, AIAA-86-0969-CP, Pt. 1, pp. 442–452.

[21] Armanios, E. A., and Rehfield, L. W., "A Simplified Approach to Strain Energy Release Computations for Interlaminar Fracture of Composites," *Proceedings of the Fourth Japan-U.S. Conference on Composite Materials*, Technomic Publishing Co., Washington, D.C., 1988, pp. 285–296.

[22] Rehfield, L. W., Armanios, E. A., and Weinstein, F., "Analytical Modeling of Interlaminar Fracture in Laminated Composites," Composites '86: Recent Advances in Japan and the United States, *Proceedings of the Third Japan-U.S. Conference on Composite Materials*, edited by K. Kawata, S. Umekawa, and A. Kobayashi, Japan Society for Composite Materials, Tokyo, Japan, 1986, pp. 331–340.

[23] "Standard Test Method for Strength Properties of Adhesives in Shear by Tension Loading of Single-Lap-Joint Laminated Assemblies," American Society for Testing and Materials ASTM D3165-95, 1995, pp. 199–202.

[24] Maple 9.52, Waterloo Maple Inc., Ontario, Canada, 2005.

[25] Rybicki, E. F., and Kanninen, M. F., "A Finite Element Calculation of Stress Intensity Factors by a Modified Crack Closure Integral," *Engineering Fracture Mechanics*, Vol. 9, No. 4, 1977, pp. 931–938. doi:10.1016/0013-7944(77)90013-3

[26] Raju, I. S., "Calculation of Strain-Energy Release Rates With Higher Order and Singular Finite Elements," *Engineering Fracture Mechanics*, Vol. 28, No. 3, 1987, pp. 251–274. doi:10.1016/0013-7944(87)90220-7

[27] Anderson, T. L., *Fracture Mechanics: Fundamentals and Applications*, 3rd ed., CRC Press, Boca Raton, FL, 2005.

[28] Barsoum, R. S., "On the Use of Iso-Parametric Finite Elements in Linear Fracture Mechanics," *International Journal for Numerical Methods in Engineering*, Vol. 10, No. 1, 1976, pp. 25–37. doi:10.1002/nme.1620100103

[29] Henshell, R. D., and Shaw, K. G., "Crack Tip Finite Elements are Unnecessary," *International Journal for Numerical Methods in Engineering*, Vol. 9, No. 3, 1975, pp. 495–507. doi:10.1002/nme.1620090302